

Kullback–Leibler Divergence-Based Fuzzy C-Means Clustering Incorporating Morphological Reconstruction and Wavelet Frames for Image Segmentation

Cong Wang[✉], Member, IEEE, Witold Pedrycz[✉], Life Fellow, IEEE, ZhiWu Li[✉], Fellow, IEEE, and MengChu Zhou[✉], Fellow, IEEE

Abstract—In this article, we elaborate on a Kullback–Leibler (KL) divergence-based Fuzzy C-Means (FCM) algorithm by incorporating a tight wavelet frame transform and morphological reconstruction (MR). To make membership degrees of each image pixel closer to those of its neighbors, a KL divergence term on the partition matrix is introduced as a part of FCM, thus resulting in KL divergence-based FCM. To make the proposed FCM robust, a filtered term is augmented in its objective function, where MR is used for image filtering. Since tight wavelet frames provide redundant representations of images, the proposed FCM is performed in a feature space constructed by tight wavelet frame decomposition. To further improve its segmentation accuracy (SA), a segmented feature set is reconstructed by minimizing the inverse process of its objective function. Each reconstructed feature is reassigned to the closest prototype, thus modifying abnormal features produced in the reconstruction process. Moreover, a segmented image is reconstructed by using tight wavelet frame reconstruction. Finally, supporting experiments coping with synthetic, medical, and real-world images are reported. The experimental results exhibit that the proposed algorithm works well and comes with better

Manuscript received 13 January 2020; revised 26 April 2021; accepted 11 July 2021. Date of publication 8 October 2021; date of current version 19 July 2022. This work was supported in part by the China National Postdoctoral Program for Innovative Talents under Grant BX2021249; in part by the National Natural Science Foundation of China under Grant 61873342, Grant 61672400, and Grant 62076189; in part by the Recruitment Program of Global Experts; and in part by the Science and Technology Development Fund, MSAR, under Grant 0012/2019/A1. This article was recommended by Associate Editor A. F. Skarmeta Gómez. (Corresponding authors: ZhiWu Li; MengChu Zhou.)

Cong Wang is with the School of Artificial Intelligence, Optics and Electronics, Northwestern Polytechnical University, Xi'an 710072, China (e-mail: congwang0705@nwpu.edu.cn).

Witold Pedrycz is with the Department of Electrical and Computer Engineering, University of Alberta, Edmonton, AB T6R 2V4, Canada, also with the School of Electro-Mechanical Engineering, Xidian University, Xi'an 710071, China, and also with the Faculty of Engineering, King Abdulaziz University, Jeddah 21589, Saudi Arabia (e-mail: wpedrycz@ualberta.ca).

ZhiWu Li is with the School of Electro-Mechanical Engineering, Xidian University, Xi'an 710071, China, and also with the Institute of Systems Engineering, Macau University of Science and Technology, Macau, China (e-mail: zhwl@xidian.edu.cn).

MengChu Zhou is with the Helen and John C. Hartmann Department of Electrical and Computer Engineering, New Jersey Institute of Technology, Newark, NJ 07102 USA, and also with the Institute of Systems Engineering, Macau University of Science and Technology, Macau, China (e-mail: zhou@njit.edu).

Color versions of one or more figures in this article are available at <https://doi.org/10.1109/TCYB.2021.3099503>.

Digital Object Identifier 10.1109/TCYB.2021.3099503

segmentation performance than other peers. In a quantitative fashion, its average SA improvements over its peers are 4.06%, 3.94%, and 4.41%, respectively, when segmenting synthetic, medical, and real-world images. Moreover, the proposed algorithm requires less time than most of the FCM-related algorithms.

Index Terms—Fuzzy C-means (FCMs), image segmentation, Kullback–Leibler divergence, morphological reconstruction (MR), wavelet frame.

I. INTRODUCTION

Due to its simplicity, a Fuzzy C-Means (FCM) algorithm [1], [2] has been applied to a wide range of applications, such as image analysis [3], granular computing [4], and pattern recognition [5]. However, the conventional FCM algorithm only performs well for noise-free image data [3]. To overcome its drawback, a collection of improved FCM versions has been proposed by mainly considering spatial information [6]–[10] and kernel distances (functions) [11]–[15] as their parts.

For the first improvement, Ahmed *et al.* [6] reported an improved algorithm, namely, FCM_S, by introducing a neighbor term into the FCM algorithm. Since FCM_S calculates the neighbor term in each iteration, its computational complexity is high. To speed up clustering process, Chen and Zhang [7] introduced its two variants, namely: 1) FCM_S1 and 2) FCM_S2, by employing mean and median filters, respectively. However, such two algorithms do not work well for Gaussian or other well-known noise. Cai *et al.* [8] proposed a fast generalized FCM algorithm (FGFCM) by using gray-level histograms. However, its drawback is to require more parameter settings. Krinidis and Chatzis [9] utilized a fuzzy factor to simplify the parameter settings in FGFCM, thus forming a fuzzy local information C-means algorithm (FLICM). Nevertheless, it is not effective for arbitrary spatial information since it only adopts the nonrobust Euclidean distance.

To further enhance FLICM's robustness, the second improvement is investigated by augmenting kernel distances into FLICM's objective function, thus resulting in a collection of kernel-based FCM algorithms [11]–[15]. Typically, Gong *et al.* [11] introduced a tradeoff weighted fuzzy factor and a kernel metric to improve FLICM's robustness,

thus forming a novel algorithm, namely, KWFLICM. This algorithm works well for different types of noise, but it is extremely time consuming. Zhao *et al.* [12] proposed a neighborhood weighted FCM clustering algorithm (NWFCM) by replacing a Euclidean distance with a neighborhood weighted distance. Compared with FLICM and KWFLICM, NWFCM exhibits higher computational efficiency. However, the usage of the patch distance and setting of several parameters make NWFCM's computational overheads higher than those of many FCM-related algorithms.

For the sake of robustness improvement and computational efficiency, some comprehensive FCMs have been recently reported [16]–[25], which involve various mathematical techniques, such as Kullback–Leibler (KL) divergence [16], [17]; morphological gray reconstruction [18]–[20]; and sparse representation [22], [23]. Typically, Gharieb *et al.* [16] introduced the KL divergence to restrain local memberships, which achieved the improvement for the conventional FCM algorithm. Whereas, the derived algorithm exhibits low computational efficiency and its performance can be further improved. Lei *et al.* [18] came up with a fast and robust FCM algorithm (FRFCM) based on morphological gray reconstruction and membership filtering. FRFCM is fast due to the use of gray-level histograms. However, its performance is sometimes unstable. More recently, Zhang *et al.* [22] have proposed two alternative clustering algorithms, namely: 1) DSFCM and 2) DSFCM_N, which introduce sparse regularization in terms of deviations into the objective function of FCM. Once spatial information is encountered, DSFCM upgrades to DSFCM_N that makes full use of neighbor information. Although both algorithms provide a new avenue for image segmentation, their performance can be further improved.

By reviewing the literature, we conclude that existing algorithms cannot make a good tradeoff between the segmentation performance and speed of clustering. In other words, the improved FCM-related algorithms are not well exploited yet, which exhibit good segmentation effects and high efficiency. Generally speaking, membership grades of a specific image pixel are close to those of its neighborhoods. Hence, optimizing the membership partition in each iteration has a positive impact on FCM's performance enhancement. However, no work involves a comprehensive discussion on optimizing a partition matrix. Although the work in [16] has roughly touched on optimizing the local membership grade by using KL divergence, there lacks a further discussion on enhancing its segmentation performance and computational efficiency.

To do so, we present a KL divergence-based FCM (KLDFCM) algorithm by incorporating a tight wavelet frame transform [26], [27] and a morphological reconstruction (MR) operation [28], [29]. Its framework is portrayed in Fig. 1. Aiming to enhance FCM's robustness, an observed image is first filtered by using MR. Tight wavelet frame decomposition is employed to form feature sets associated with observed and filtered images. Taking these feature sets as data of clustering, KLDFCM is proposed, which incorporates a KL divergence term on the partition matrix into FCM's objective function. On the basis of the obtained partition matrix and prototypes, a segmented feature set is reconstructed by minimizing the inverse process of KLDFCM's objective function. To modify abnormal features produced in the

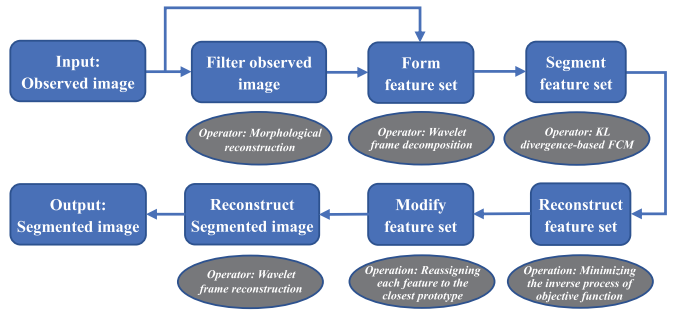


Fig. 1. Framework of the proposed algorithm.

reconstruction process, each reconstructed feature is reassigned to the closest prototype. In the sequel, KLDFCM's segmentation accuracy (SA) is further improved. Finally, a segmented image is reconstructed by using tight wavelet frame reconstruction.

This study intends to make four original contributions that:

- 1) It presents KLDFCM by introducing a KL divergence term on a partition matrix into FCM's objective function. With the assistance of the KL divergence term, membership grades of a specific image pixel are close to those of its neighborhoods. Therefore, the optimization of membership partition in each iteration yields a positive impact on the segmentation performance of FCM.
- 2) It incorporates image filtering into KLDFCM's objective function, which means that spatial information of an image is introduced into clustering and the iterative calculation of a conventional local neighbor term is avoided. MR is applied to image filtering, which avoids the issue of selecting different filters suitable for different types of noise.
- 3) It performs KLDFCM in a feature space generated by using a tight wavelet frame transform, which thereby eliminates the defect of using image pixels. Since sparse approximations of an image can be acquired in such space, the underlying features in an image can be analyzed as much as possible.
- 4) It realizes the reconstruction process of a segmented feature set by minimizing the inverse process of KLDFCM's objective function. This process further improves KLDFCM's SA.

In conclusion, this work presents a distinct originality that KLDFCM is an FRFCM by using some potential measures. It is conducted in the feature space produced by tight wavelet frames, which is useful to manipulate image features and noise. Even though KL divergence has a positive impact on the optimization of membership partition, it results in a high computing overhead. The use of MR overcomes the drawback caused by KL divergence since it acts as a preprocessing step to introduce spatial information into FCM in advance, implying that the iterative calculation of a conventional local neighbor term is completely avoided. In addition, in order to further enhance the segmentation effects, the reconstruction of the segmented feature set is performed. Finally, FCM's parameter setting is simplified since the usage of KL divergence avoids the need for the fuzzification exponent in the clustering algorithm.

The remainder of this article is organized as follows. Section II briefly describes FCM and a tight wavelet frame transform. Section III presents the proposed algorithm. Section IV reports experimental results for synthetic, medical, and color images. Finally, conclusions are drawn in Section V.

II. PRELIMINARIES

A. Fuzzy C-Means

Denote an image with K pixels as f . Since each image pixel often implies a set of attributes (variables), f can be formulated as $\mathbf{X} = \{\mathbf{x}_1, \mathbf{x}_2, \dots, \mathbf{x}_K\} \subset \mathbb{R}^K$. The FCM algorithm divides \mathbf{X} into several clusters by minimizing the objective function

$$J(\mathbf{U}, \mathbf{V}) = \sum_{i=1}^c \sum_{j=1}^K u_{ij}^m \|\mathbf{x}_j - \mathbf{v}_i\|^2 \quad (1)$$

subject to

$$\sum_{i=1}^c u_{ij} = 1, \quad \text{for } j \in \{1, 2, \dots, K\}$$

where $\mathbf{U} = [u_{ij}]_{c \times K}$ with $0 \leq u_{ij} \leq 1$ is a partition matrix, $\mathbf{V} = \{\mathbf{v}_i\}_{i=1,2,\dots,c}$ is a set of c prototypes, $\|\cdot\|$ denotes the Euclidean distance, and m is a fuzzification exponent ($m > 1$).

The minimization of (1) can be realized by iteratively updating the partition matrix and the prototypes [30]

$$u_{ij} = \frac{\left(\|\mathbf{x}_j - \mathbf{v}_i\|^2 \right)^{-\frac{1}{m-1}}}{\sum_{q=1}^c \left(\|\mathbf{x}_j - \mathbf{v}_q\|^2 \right)^{-\frac{1}{m-1}}} \quad \text{and} \quad \mathbf{v}_i = \frac{\sum_{j=1}^K u_{ij}^m \mathbf{x}_j}{\sum_{j=1}^K u_{ij}^m}.$$

By presetting a non-negative threshold ε , FCM iterates until $\|\mathbf{U}^{(t+1)} - \mathbf{U}^{(t)}\| < \varepsilon$ has been met. Here, t is an iteration index.

B. Tight Wavelet Frame Transform

Wavelet frames exhibit powerful ability for feature/textured extraction. Thus, they are applied to a wide range of research fields, such as image segmentation [13]; image denoising [31]–[33]; image restoration [26]; and mesh surface reconstruction [34], [35]. For the sake of simplicity, we introduce the main idea of a tight wavelet frame transform. The readers are referred to [26] and [27]. The tight wavelet frame transform involves two operators, that is: 1) decomposition \mathcal{W} and 2) reconstruction \mathcal{W}^T . By collecting a set of filters (masks), \mathcal{W} can be generated based on γ subfiltering operators, that is, $\mathcal{W}_0, \mathcal{W}_1, \dots, \mathcal{W}_{\gamma-1}$. Among them, \mathcal{W}_0 is the low-pass filtering operator and the rest are high-pass filtering operators. With the assistance of the unitary extension principle [36], \mathcal{W}^T can be available. Moreover, we have $\mathcal{W}^T \mathcal{W} f = f$, where $\mathcal{W}^T \mathcal{W}$ is an identity operation.

III. METHODOLOGY

A. Image Filtering via MR

As a preprocessing step, MR is applied to filter an observed image, which improves FCM's robustness and makes the distribution characteristic of image pixels favorable to fuzzy

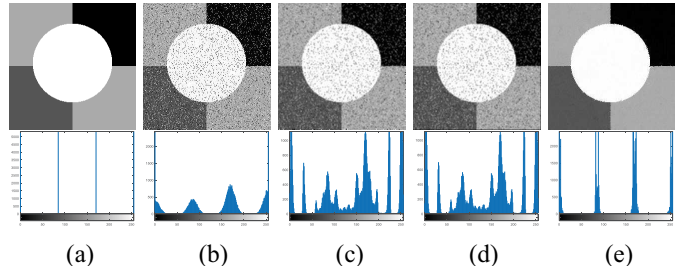


Fig. 2. Comparison with different filtering methods. (a) Original image. (b) Observed image. (c) Filtered result using a mean filter. (d) Filtered result using a median filter. (e) Filtered result using MR.

clustering. Formally speaking, MR is composed of two operators, that is: 1) dilation and 2) erosion reconstruction [37]. Given two images f (mask image) and g (marker image), the dilation reconstruction is defined as

$$\mathcal{R}_f^D(g) = \mathcal{D}_f^{(t)}(g)$$

where $\mathcal{D}_f^{(t)}(g)$ is formulated as

$$\mathcal{D}_f^{(t)}(g) = \begin{cases} \mathcal{D}(g) \ddot{\wedge} f, & t = 1 \\ \mathcal{D}(\mathcal{D}^{(t-1)}(g)) \ddot{\wedge} f, & t = 2, 3, \dots \end{cases}$$

where $g \leq f$, $\ddot{\wedge}$ stands for the pointwise minimum and \mathcal{D} represents the dilation of g by a flat structuring element [29].

The erosion reconstruction is defined as

$$\mathcal{R}_f^E(g) = \mathcal{E}_f^{(t)}(g)$$

where $\mathcal{E}_f^{(t)}(g)$ is formulated as

$$\mathcal{E}_f^{(t)}(g) = \begin{cases} \mathcal{E}(g) \ddot{\vee} f, & t = 1 \\ \mathcal{E}(\mathcal{E}^{(t-1)}(g)) \ddot{\vee} f, & t = 2, 3, \dots \end{cases}$$

where $g \geq f$, $\ddot{\vee}$ stands for the pointwise maximum and \mathcal{E} represents the erosion of g by a flat structuring element.

Here, we select $g = \mathcal{E}(f)$ and $g = \mathcal{D}(f)$ as marker images for dilation and erosion reconstructions, respectively. According to the two reconstruction operators, the morphological closing reconstruction of f is given as

$$\mathcal{R}^C(f) = \mathcal{R}_{\mathcal{R}_f^D(\mathcal{E}(f))}^E \left(\mathcal{D} \left(\mathcal{R}_f^D(\mathcal{E}(f)) \right) \right). \quad (2)$$

In this work, f is an observed image and its filtered image is denoted as $\tilde{f} = \mathcal{R}^C(f)$.

To illustrate MR's performance for feature preservation and noise suppression, we give an example (refer to Fig. 2). A square of size 3×3 is the structuring element.

The first row of Fig. 2 shows an original image, an observed image, and three filtered images generated by a mean filter, a median filter, and MR, respectively. The second row of Fig. 2 represents the corresponding gray-level histograms. The original image includes four gray levels, that is, 0, 85, 170, and 255. Obviously, its gray-level histogram has four obvious peaks. We generate the observed image by imposing mixed Gaussian and impulse noise (MGIN) with $s = 10$ and $r = 10\%$ (additive white Gaussian noise with standard deviation s and salt and pepper impulse noise with density r) on the original image. The gray level histogram of the observed

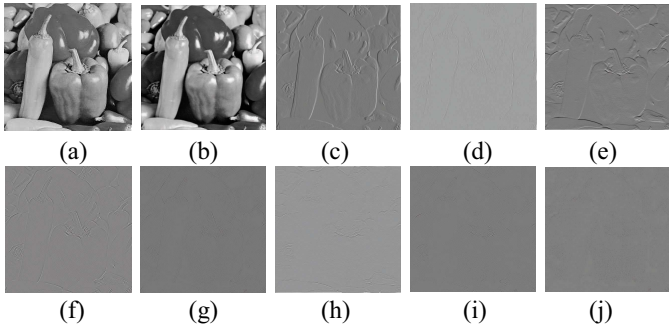


Fig. 3. Original image f and its wavelet coefficients. (a) Original image f . (b)–(j) $\mathcal{W}_0f, \mathcal{W}_1f, \dots, \mathcal{W}_8f$.

image only has two apparent peaks (0 and 255). As shown in Fig. 2(c) and (d), both mean and median filters produce too many peaks while MR mainly splits the observed image into four clusters. Thus, MR can effectively retain image details and remove noise simultaneously.

B. Feature Extraction via Wavelet Frames

On the basis of the observed image and filtered image generated by MR, we can employ a tight frame system to form their feature sets. In many applications, a piecewise linear B-spline tight frame system [36], [38] is shown to be more adaptable to features and noise since it can provide redundant representations of images. Thus, we choose this system in which the corresponding filters are discretized as

$$a_0 = \left[\frac{1}{4}, \frac{1}{2}, \frac{1}{4} \right], a_1 = \left[-\frac{1}{4}, \frac{1}{2}, -\frac{1}{4} \right], a_2 = \left[\frac{\sqrt{2}}{4}, 0, -\frac{\sqrt{2}}{4} \right].$$

Using the above three 1-D filters, we generate nine 2-D filters, including one low-pass filter and eight high-pass filters, which correspond to nine subfiltering operators $\mathcal{W}_0, \mathcal{W}_1, \dots, \mathcal{W}_8$. They make up a tight wavelet frame decomposition operator \mathcal{W} . Hence, we can utilize the decomposition operator to form feature sets associated with the observed and filtered images, that is

$$\mathcal{X} = \mathcal{W}f \text{ and } \bar{\mathcal{X}} = \mathcal{W}\bar{f}. \quad (3)$$

For image processing, \mathcal{W}_0f and $\mathcal{W}_0\bar{f}$ represent low-frequency information, and the rest represent high-frequency information. The above formulation abstracts the feature extraction results obtained by the use of 1-level tight wavelet frame decomposition. The value of the decomposition level represents the number of times where the target data are sequentially decomposed. To better exhibit the effect of wavelet frames, we show an example (refer to Fig. 3).

As shown in Fig. 3, we find that 1-level tight wavelet frame decomposition gives redundant representations of a sampled image, thus forming a feature set of the image. The dimensionality of the feature set is nine times higher than the one of the sampled image. That is to say, each image pixel contains nine underlying attributes, that is, one low frequency and eight high frequencies. Formally speaking, for an image with K pixels, the size of its feature set \mathcal{X} is $9 \times K$. Therefore, for

image segmentation, the dimensionality of data of clustering is expanded when compared with the direct use of image pixels.

C. KL Divergence-Based FCM

By introducing spatial information and tight wavelet frames, FCM becomes more robust to noise. We reformulate feature sets associated with f and \bar{f} as $\mathcal{X} = \mathcal{W}f = \{x_j : j = 1, 2, \dots, K\}$ and $\bar{\mathcal{X}} = \mathcal{W}\bar{f} = \{\bar{x}_j : j = 1, 2, \dots, K\}$. In fact, membership grades of a specific image pixel are close to those of its neighborhoods. Hence, optimizing FCM's partition matrix in each iteration has a positive impact on FCM's segmentation performance. In this article, we use a KL divergence distance D_{KL} to characterize the difference of membership partition between a target pixel x_j and its neighborhoods. Clearly, the distance $D_{KL}(u_{ij}, \bar{u}_{ij})$ should approximate to zero, that is, $D_{KL}(u_{ij}, \bar{u}_{ij}) \rightarrow 0$, where u_{ij} is a membership grade stating that x_j belongs to the i th cluster, and \bar{u}_{ij} stands for a median value of membership grades stating that neighborhoods of x_j belong to the i th cluster. Therefore, we can impose a constraint on FCM's objective function as follows

$$J(\mathbf{U}, \mathbf{V}) = \sum_{i=1}^c \sum_{j=1}^K u_{ij} \left(\|x_j - v_i\|^2 + \alpha \|\bar{x}_j - v_i\|^2 \right)$$

such that

$$D_{KL}(\mathbf{U}, \bar{\mathbf{U}}) = \sum_{i=1}^c \sum_{j=1}^K u_{ij} \log \frac{u_{ij}}{\bar{u}_{ij}} = 0$$

where α is a positive parameter that controls the impact of a filtered term $\|\bar{x}_j - v_i\|^2$ on FCM. In the sequel, the objective function of KLDFCM is expressed as

$$J(\mathbf{U}, \mathbf{V}) = \sum_{i=1}^c \sum_{j=1}^K u_{ij} \left(\|x_j - v_i\|^2 + \alpha \|\bar{x}_j - v_i\|^2 \right) + \beta \sum_{i=1}^c \sum_{j=1}^K u_{ij} \log \frac{u_{ij}}{\bar{u}_{ij}} \quad (4)$$

where β is a positive parameter that controls the impact of the KL divergence term $D_{KL}(\mathbf{U}, \bar{\mathbf{U}})$ on FCM. Note that the fuzzification exponent m is not present in (4). The KL divergence term $D_{KL}(\mathbf{U}, \bar{\mathbf{U}})$ involves an original partition matrix $\mathbf{U} = [u_{ij}]_{c \times K}$ and a filtered partition matrix $\bar{\mathbf{U}} = [\bar{u}_{ij}]_{c \times K}$ that is defined as

$$\bar{\mathbf{U}} = \text{median}(\mathbf{U}). \quad (5)$$

Here, the operator median represents median filtering applied to each row of \mathbf{U} with a local window of a selected size, which means that abnormal membership grades in \mathbf{U} produced in each iteration are modified by their neighbors.

In particular, in [16], KL divergence is first introduced into FCM's objective function. However, being different from our work, a mean filter is employed for constructing the KL divergence term. The mean filtering results are experimentally worse than median filtering ones. Furthermore, the work in [16] shows two shortcomings that: 1) the usage of KL divergence results in high computational complexity and 2) a robust kernel distance is absent. In our work, the use of MR and tight wavelet frames overcomes such shortcomings.

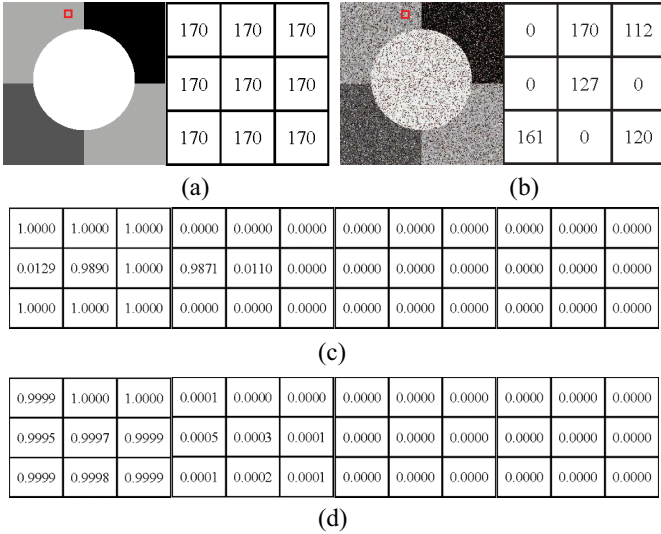


Fig. 4. Comparison of partition matrices generated by FCM and KLDFCM. (a) Original image. (b) Observed image. (c) Partition matrix using FCM. (d) Partition matrix using KLDFCM.

We apply the Lagrange multiplier method to minimize (4). The iterative updates of the partition matrix \mathbf{U} and prototypes \mathbf{v}_i are given as follows:

$$u_{ij} = \frac{\bar{u}_{ij} e^{-(\|x_j - v_i\|^2 + \alpha \|\bar{x}_j - v_i\|^2)/\beta}}{\sum_{q=1}^c \bar{u}_{qj} e^{-(\|x_j - v_q\|^2 + \alpha \|\bar{x}_j - v_q\|^2)/\beta}} \quad (6)$$

$$v_i = \frac{\sum_{j=1}^K u_{ij} (x_j + \alpha \bar{x}_j)}{(1 + \alpha) \sum_{j=1}^K u_{ij}}. \quad (7)$$

The detailed derivations are provided in the Appendix.

We cover an example to illustrate the impact of the KL divergence on FCM. We impose MGIN on an original image shown in Fig. 2(a). The noise level is set to $s = 30$ and $r = 20\%$. To better exhibit the impact of the KL divergence, we fix $\alpha = 1.5$ while the 1-level tight wavelet frame decomposition is present. The number of clusters is set to 4 since the original image contains four gray levels. As shown in Fig. 4, by introducing the KL divergence and setting $\beta = 15\,000$ (how to select the value of β will be discussed in Section IV-A), an arbitrary image pixel has close membership grades to those of its neighbors, which means that the membership partition becomes more suitable and classification errors are reduced.

D. Reconstruction of Segmented Feature Set

To further improve KLDFCM's performance, we conduct the reconstruction for a segmented feature set. We denote the obtained partition matrix and prototypes as $\mathbf{U}^* = [u_{ij}^*]_{c \times K}$ and $\mathbf{V}^* = [v_i^*]_{1,2,\dots,c}$. Based on them, we obtain a segmented feature set $\tilde{\mathbf{X}}$ that contains c prototypes. A filtered partition matrix corresponding to \mathbf{U}^* is denoted as $\bar{\mathbf{U}}^* = [\bar{u}_{ij}^*]_{c \times K}$. By their assistance, we reconstruct the segmented feature set by minimizing the inverse process of (4), that is

$$J(\tilde{\mathbf{X}}) = \sum_{i=1}^c \sum_{j=1}^K u_{ij}^* (\|\tilde{x}_j - v_i^*\|^2 + \alpha \|\bar{x}_j - v_i^*\|^2) + \beta \sum_{i=1}^c \sum_{j=1}^K u_{ij}^* \log \frac{u_{ij}^*}{\bar{u}_{ij}^*} \quad (8)$$

where $\tilde{\mathbf{X}} = \{\tilde{x}_j\}_{j=1,2,\dots,K}$ is a reconstructed feature set and $\sum_{i=1}^c u_{ij}^* = 1$ always holds. Obviously, there exists an unknown $\tilde{\mathbf{X}}$ in (8). Thus, we can acquire reconstructed feature set $\tilde{\mathbf{X}}$ by solving

$$\frac{\partial J}{\partial \tilde{x}_j} = 0.$$

The optimal \tilde{x}_j is presented as

$$\tilde{x}_j = \sum_{i=1}^c u_{ij}^* v_i^*. \quad (9)$$

In the reconstruction process, some differences between $\tilde{\mathbf{X}}$ and $\hat{\mathbf{X}}$ are encountered, which are produced by abnormal features in $\tilde{\mathbf{X}}$ that do not belong to $\hat{\mathbf{X}}$. To modify these features, for $j = 1, 2, \dots, K$, we substitute \tilde{x}_j by \hat{x}_j defined as

$$\hat{x}_j = v_i^*, \text{ for } i \in \{1, 2, \dots, c\} \quad (10)$$

subject to

$$\|\tilde{x}_j - v_i^*\| = \min\{\|x_j - v_1^*\|, \dots, \|x_j - v_c^*\|\}.$$

All elements $\{\hat{x}_j\}_{j=1,2,\dots,K}$ make up a modified feature set $\hat{\mathbf{X}}$.

To intuitively show the effect of the reconstruction process, we take a case in which tight wavelet frames are absent. We choose a noisy image, as shown in Fig. 4(b). We set $c = 4$, $\alpha = 1.5$, and $\beta = 15\,000$. The obtained results are displayed in Fig. 5.

Fig. 5 indicates the segmentation result obtained by using KL divergence is unsatisfactory to certain extent. In the reconstruction process, some blurred edges are produced. Thus, the reconstructed image contains more than four gray levels. Whereas, these blurred edges are eliminated in the modification process.

E. Reconstruction of Segmented Image

Once the modified feature set is obtained, we reconstruct a segmented image \tilde{f} by using tight wavelet frame reconstruction \mathcal{W}^T , i.e.,

$$\tilde{f} = \mathcal{W}^T(\hat{\mathbf{X}}). \quad (11)$$

The proposed algorithm is realized as Algorithm 1.

IV. EXPERIMENTAL STUDIES

In this section, we complete a collection of numerical experiments to verify the effectiveness and efficiency of the proposed algorithm. We provide KLDFCM's segmentation results reported for synthetic, medical, and real-world images. Moreover, we also make some comparisons between KLDFCM and eight existing algorithms in the literature, including "FCM_S1" [7], "FCM_S2" [7], "FGFCM" [8], "FLICM" [9], "KWFLICM" [11], "FRFCM" [18], "WFCM" [13], and "DSFCM_N" [22].

Besides visual comparisons, we display segmentation comparisons in a quantitative fashion. Here, we employ eight performance indicators, that is: 1) SA [11]; 2) accuracy (Acc) [39]; 3) sensitivity (Sen) [40]; 4) specificity (Spe) [41];

Algorithm 1 KLDFCM Algorithm Incorporating MR and Wavelet Frames

Input: Observed image f , number of clusters c , and threshold ε .

Output: Segmented image \tilde{f} .

- 1: Calculate the filtered image \bar{f} via (2)
- 2: Calculate the feature sets X and \bar{X} via (3)
- 3: Initialize randomly the filtered partition matrix $\bar{U}^{(0)}$ and prototypes $V^{(0)}$
- 4: $t \leftarrow 0$
- 5: **repeat**
- 6: Calculate the partition matrix $U^{(t+1)}$ using the filtered partition matrix $\bar{U}^{(t)}$ and prototypes $V^{(t)}$ via (6)
- 7: Update the filtered partition matrix $\bar{U}^{(t+1)}$ via (5)
- 8: Update the prototypes $V^{(t+1)}$ by using the partition matrix $U^{(t+1)}$ via (7)
- 9: $t \leftarrow t + 1$
- 10: **until** $\|U^{(t+1)} - U^{(t)}\| < \varepsilon$
- 11: **return** partition matrix U , prototypes V , and filtered partition matrix \bar{U}
- 12: Calculate the reconstructed feature set \tilde{X} via (9)
- 13: Calculate the modified feature set \hat{X} via (10)
- 14: Calculate the segmented image \tilde{f} via (11)

5) entropy-based information (EI) [42]; 6) partition coefficient (PC) [2]; 7) partition entropy (PE) [43]; and 8) Xie and Beni's Index (XB) [44]. SA, Acc, Sen, and Spe are often used to assess the performance of segmenting synthetic images with known ground truth. The larger their values are, the better the segmentation effect becomes. EI is usually employed to evaluate the results for segmenting images without ground truth. Its essence is to minimize the uniformity across all clusters by maximizing the uniformity of pixels within each segmented cluster. Hence, the better segmentation effect is associated with a smaller EI value. The remaining indicators are used to evaluate the cluster validity of FCM-related algorithms. For all experiments, the best results are shown in boldface.

A. Parameter Setting

Before conducting all numerical experiments, we introduce parameter settings in all algorithms. Since all comparative algorithms take spatial information of observed images into account, we fairly select a local window with size 3×3 . We set fuzzification exponent $m = 2$ across eight comparative algorithms, and threshold $\varepsilon = 1 \times 10^{-6}$ across all algorithms. The number of clusters c is assumed to be known, and preset to the same value for all algorithms. It is noted that KLDFCM is free of m .

Except for m , ε , and c , we introduce how to set the remaining parameters in all comparative algorithms. α in FCM_S1 and FCM_S2 is experimentally set to 3.8, which is used to control the impact of the neighborhood term on FCM. In FGFCM, we set the spatial scale factor λ_s and the gray-level scale factor λ_g to 3 and 5, respectively. There exist no more parameters in FLICM and KWFLICM. For FRFCM, an observed image is selected as the mask image and the marker image is

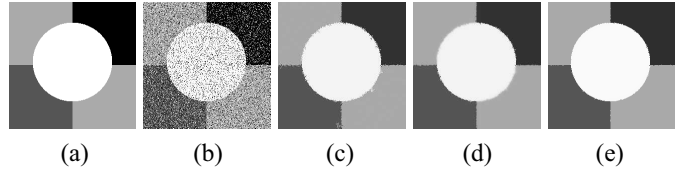


Fig. 5. Investigation of the reconstruction process. (a) Original image. (b) Observed image. (c) Segmented image via KL divergence. (d) Reconstructed image. (e) Modified image.

obtained by a square structuring element of size 3×3 . What is more, a median filter with window size 3×3 is applied to the fuzzy membership filtering. As to WFCM, μ controls the impact of the spatial information on FCM, which is determined experimentally with the values in range of [0.55, 0.65]. For DSFCM_N, p is set to 1 and the parameter vector λ is selected according to the standard deviation of each channel of image data.

Next, we discuss how to set the remaining parameters in KLDFCM. To apply MR to filter image pixels, we select the same parameters as those in FRFCM. For the tight wavelet frame transform, we set its level to 1. A median filter with window size 3×3 is applied to the membership filtering. Beyond that, there only exist two parameter α and β in KLDFCM. Here, we report two examples to exhibit how to select α and β . We impose MGIN with $s = 30$ and $r = 20\%$ on three synthetic images with ground truth [refer to Fig. 6(a)–(c)]. By fixing $\beta = 15\,000$ in advance, we first take a set of values of α to show the change of segmentation performance of the proposed algorithm. As shown in Fig. 7, with the increase of α , the Acc value keeps increasing until it reaches the maximum. After that, the Acc value slowly decreases. In order to provide a reference for parameter selection in the following experiments, we can determine α experimentally within the range [0.5, 1.5].

For selection of β , by fixing $\alpha = 1$, we take a sequence of values of β to investigate their impacts on the segmentation effects of the proposed algorithm. β is increased from an initial value. Here, we set the initial value to 5000 for all tested examples. As shown in Fig. 8, there exists a maximum of Acc as β increases. To simplify parameter settings of the following experiments, we choose $\beta \in [10\,000, 45\,000]$ experimentally.

B. Ablation Studies and Analysis

The proposed algorithm involves four key components, that is: 1) image filtering; 2) feature extraction; 3) KL divergence; and 4) feature set reconstruction. In the following, we conduct ablation studies to exhibit the impact of each component on the proposed algorithm. The MGIN with $s = 30$ and $r = 20\%$ is imposed on the image shown in Fig. 6(b). The number of clusters is set to 4. We select $\alpha = 1$ and $\beta = 15\,000$. The level of tight wavelet frame transform is 1. The results are displayed in Table I, which are obtained after several runs. The symbol \checkmark represents the corresponding component is enabled while symbol \times indicates that the corresponding component becomes absent.

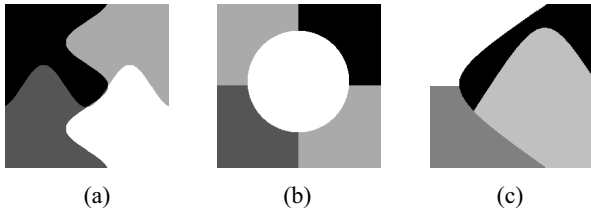


Fig. 6. Three synthetic images with ground truth.

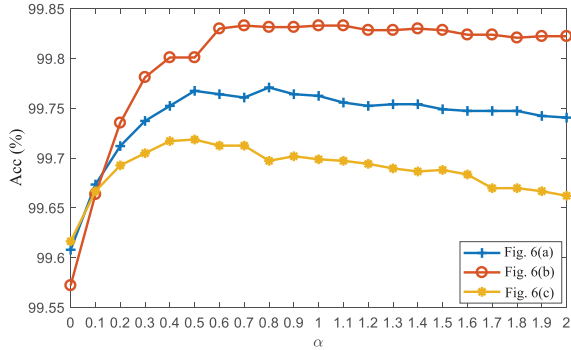
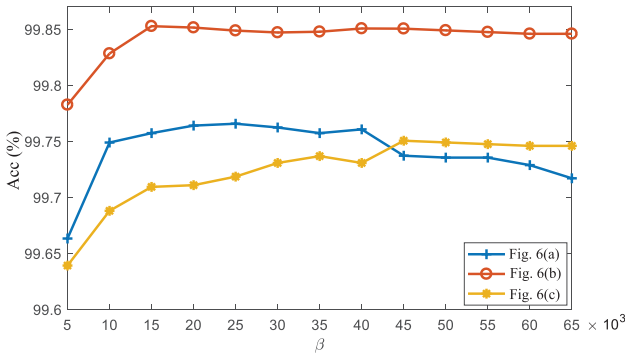
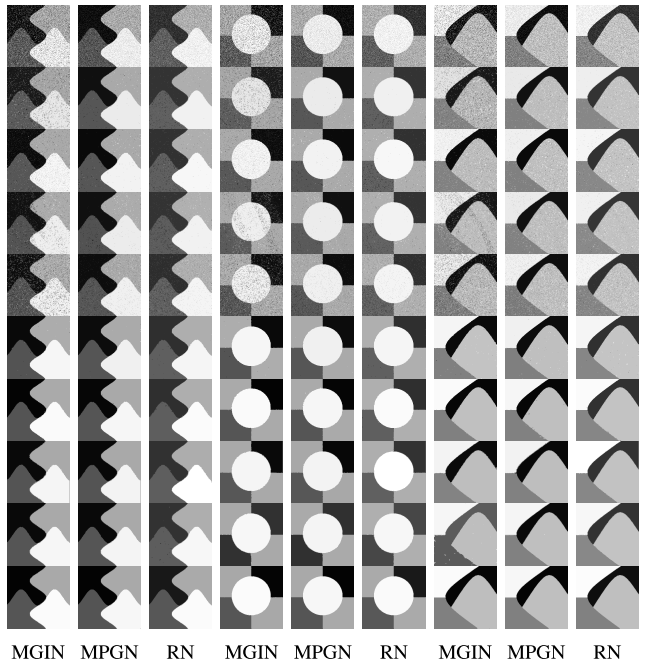
Fig. 7. Accuracy versus values of α .Fig. 8. Accuracy versus values of β .TABLE I
INVESTIGATION OF EACH COMPONENT IN THE PROPOSED ALGORITHM

Image filtering	Feature extraction	KL divergence	Feature set reconstruction	Acc (%)	Iterations
×	×	×	×	91.9734	27
✓	×	×	×	98.7976	46
×	✓	×	×	92.5247	23
×	×	✓	×	99.6536	112
×	×	✗	✓	92.4194	27
✓	✓	✓	✗	99.7528	129
✓	✓	✗	✓	98.7976	46
✓	✗	✓	✓	99.6811	119
×	✓	✓	✓	99.6536	112
✓	✓	✓	✓	99.8513	129

We test ten different combinations of the four key components. Here, we clarify that a small value of β is chosen, that is, $\beta = 60$, in order to make (6) executable, which represents that KL divergence is absent. When all components are absent, the Acc result of FCM is only 91.9734%. By considering each component alone, we can find the Acc values are increased by 6.8242%, 0.5513%, 7.6802%, and 0.4460%, respectively. Therefore, compared with feature extraction and feature set reconstruction, image filtering

Fig. 9. Segmentation results on synthetic images. The parameters (from left to right): $\alpha_1 = 0.8$, $\beta_1 = 25\ 000$; $\alpha_2 = 0.5$, $\beta_2 = 15\ 000$; $\alpha_3 = 1$, $\beta_3 = 15\ 000$; $\alpha_4 = 0.7$, $\beta_4 = 15\ 000$; $\alpha_5 = 1.5$, $\beta_5 = 20\ 000$; $\alpha_6 = 1.5$, $\beta_6 = 15\ 000$; $\alpha_7 = 0.5$, $\beta_7 = 45\ 000$; $\alpha_8 = 1$, $\beta_8 = 35\ 000$; and $\alpha_9 = 0.5$, $\beta_9 = 40\ 000$. From left to right: MGIN, MPGN, and RN. From top to bottom: noisy images and results of FCM_S1, FCM_S2, FGFCM, FLICM, KWFLICM, FRFCM, WFCM, DSFCM_N, and KLDFCM.

has a relatively larger influence on FCM's performance improvement. Except for KL divergence, other three components are time saving. In addition, KL divergence has the greatest impact on FCM's performance improvement. However, it also gives rise to high computation costs. Nevertheless, the computational efficiency of the proposed algorithm is still very high since spatial information is not computed in each iteration, which thanks to the use of MR.

C. Results for Synthetic Images

We first conduct numerical experiments of segmenting three synthetic images (see Fig. 6). Their numbers of clusters are all set to 4. To exhibit KLDFCM's robustness to multiple noise, we impose mixed Gaussian and impulse noise (MGIN, with noise level: $s = 30$ and $r = 15\%$), mixed Poisson–Gaussian noise (MPGN, with noise level: $s = 40$), and Rician noise (RN, with noise level being 40%) on all images, respectively. In particular, we remove salt and pepper impulse noise since it is one of the most common types of impulse noise. The segmentation results are illustrated in Fig. 9 and Table II.

As shown in Fig. 9, we clearly observe that FCM_S1, FCM_S2, FGFCM, and FLICM are not capable to suppress high-level noise. In comparison, KWFLICM and DSFCM_N can remove a large proportion of noise. Even though FRFCM and WFCM exhibit the superior performance for noise removal, they change image edges to some extent. Superior to these comparative algorithms, KLDFCM can efficiently remove high-level noise and preserve clear image details. Table II reports the quantitative results for segmenting synthetic images. In the presence of high-level noise,

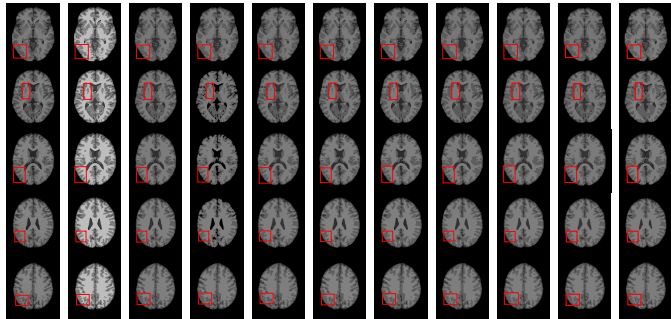


Fig. 10. Segmentation results on medical images. The parameters: $\alpha = 0.8$ and $\beta = 10\,000$. From left to right: noisy images, ground truth, and results of FCM_S1, FCM_S2, FGFCM, FLICM, KWFLICM, FRFCM, WFCM, DSFCM_N, and KLDFCM.

TABLE II
AVERAGE SEGMENTATION RESULTS ON SYNTHETIC IMAGES

Method	Noise type	SA	Acc	Sen	Spe	PC	PE	XB
FCM_S1	MGIN	0.8599	0.9751	0.9771	0.9592	0.6961	0.5836	0.3908
	MPGN	0.9726	0.9964	0.9972	0.9916	0.7953	0.4097	0.2301
	RN	0.9699	0.9303	0.9160	0.9976	0.7839	0.4299	0.2984
FCM_S2	MGIN	0.9339	0.9879	0.9886	0.9830	0.8003	0.3991	0.2765
	MPGN	0.9712	0.9971	0.9978	0.9948	0.7961	0.4073	0.1936
	RN	0.9673	0.9286	0.9139	0.9974	0.7831	0.4300	0.2631
FGFCM	MGIN	0.8886	0.9770	0.9823	0.9501	0.8420	0.3121	6.4493
	MPGN	0.9592	0.9948	0.9966	0.9865	0.8745	0.2556	7.4429
	RN	0.9569	0.9293	0.9151	0.9959	0.8677	0.2674	11.9996
FLICM	MGIN	0.8151	0.8730	0.8561	0.9510	0.6512	0.6553	0.2449
	MPGN	0.9289	0.9274	0.9127	0.9928	0.7407	0.5007	0.1247
	RN	0.9223	0.9247	0.9085	0.9943	0.7247	0.5290	0.1529
KWFLICM	MGIN	0.9963	0.9988	0.9989	0.9982	0.7495	0.5157	0.4791
	MPGN	0.9967	0.9996	0.9997	0.9993	0.8057	0.4131	0.2142
	RN	0.9959	0.9329	0.9186	0.9994	0.7850	0.4518	0.2882
FRFCM	MGIN	0.9972	0.9988	0.9990	0.9979	0.7128	0.5978	0.6205
	MPGN	0.9975	0.9995	0.9996	0.9991	0.6540	0.6988	0.2028
	RN	0.9969	0.9331	0.9190	0.9995	0.6575	0.6907	0.3102
WFCM	MGIN	0.9902	0.9968	0.9991	0.9897	0.7204	0.5542	0.4750
	MPGN	0.9908	0.9961	0.9969	0.9900	0.8098	0.4030	0.2292
	RN	0.9907	0.9320	0.9173	0.9986	0.7811	0.4584	0.4360
DSFCM_N	MGIN	0.9905	0.9327	0.9201	0.9939	0.7960	0.3843	0.8125
	MPGN	0.9895	0.9964	0.9986	0.9889	0.8531	0.3030	0.2740
	RN	0.9892	0.9301	0.9168	0.9957	0.8313	0.3447	0.3339
KLDFCM	MGIN	0.9982	0.9991	0.9987	0.9987	0.9923	0.0130	0.2511
	MPGN	0.9987	0.9998	0.9999	0.9994	0.9922	0.0132	0.0445
	RN	0.9989	0.9981	0.9993	0.9997	0.9916	0.0142	0.0596

the superiority of KLDFCM is apparent. Compared with KLDFCM, other peers mostly reveal the worse segmentation results and cluster validity. For synthetic images, the average SA improvement of KLDFCM over its peers is 4.06%.

D. Results for Medical Images

In this section, we segment magnetic resonance images (MRIs) coming from a simulated brain database (BrainWeb).¹ MRIs are generated by T1 modality with slice thickness of 1-mm resolution, 9% noise, and 20% intensity nonuniformity. As shown in Fig. 10, we select five slices in the axial plane with the sequence of 70, 80, 90, 100, and 110.

¹<http://www.bic.mni.mcgill.ca/brainweb/>

TABLE III
AVERAGE SEGMENTATION RESULTS ON MEDICAL IMAGES

Method	Segmentation						
	SA	Acc	Sen	Spe	PC	PE	XB
FCM_S1	0.7887	0.9791	0.9805	0.9795	0.8883	0.2170	0.0736
FCM_S2	0.7890	0.9861	0.9784	0.9915	0.8945	0.2060	0.0739
FGFCM	0.7859	0.9739	0.9727	0.9761	0.9073	0.1787	4.8847
FLICM	0.7828	0.9860	0.9815	0.9893	0.8732	0.2425	0.0560
KWFLICM	0.7830	0.9855	0.9891	0.9828	0.8725	0.2545	0.0783
FRFCM	0.7893	0.9832	0.9817	0.9842	0.7849	0.4164	0.0967
WFCM	0.7856	0.9665	0.9875	0.9511	0.8470	0.2913	0.0983
DSFCM_N	0.7908	0.9448	0.9946	0.9087	0.8595	0.2707	0.1193
KLDFCM	0.8179	0.9973	0.9990	0.9952	0.9760	0.0406	0.0438

TABLE IV
AVERAGE SEGMENTATION RESULTS ON REAL-WORLD IMAGES IN BSDS300

Method	EI	PC	PE	XB
FCM_S1	2.0607	0.8365	0.3260	0.3298
FCM_S2	2.0647	0.8360	0.2315	0.3310
FGFCM	2.0830	0.8390	0.2115	0.3071
FLICM	2.0904	0.8425	0.2010	0.2968
KWFLICM	2.1060	0.8325	0.2310	0.2917
FRFCM	2.0080	0.9025	0.1395	0.0983
WFCM	2.0041	0.9015	0.1305	0.1166
DSFCM_N	2.1327	0.8465	0.2060	0.2910
KLDFCM	1.9767	0.9455	0.0710	0.0371

Fig. 10 shows visual comparisons for segmenting five MRIs. The numbers of clusters are set to 4. The corresponding quantitative comparison are summarized in Table III. As shown in Fig. 10, KLDFCM maintains clear contours in images while other FCM-related algorithms generate several shape changes, such as merging and splitting. Table III shows that KLDFCM universally acquires the better evaluation results than its peers. Therefore, we conclude that KLDFCM is superior to its peers when segmenting medical images. In a quantitative fashion, the average SA improvement of KLDFCM over its peers is 3.94%.

E. Results for Real-World Images

Besides synthetic and medical images, we consider a series of real-world (color) images. Generally speaking, most of FCM-related algorithms are not applicable to color image segmentation since spatial information of color images is hard to acquire. KLDFCM overcomes this shortcoming. In addition, we can easily extend it to color image segmentation. The multivariate MR can be applied to color images [45]. As to the tight wavelet frame transform, we apply it to feature extraction in each channel of an RGB color image. Hence, the dimensionality of the obtained feature set is triple that of a gray image. The remaining operations of color image segmentation are similar to those of gray image segmentation. To further demonstrate the performance for color image segmentation, we segment two sets of real-world images next.

We first segment real-world images coming from the Berkeley Segmentation Dataset (BSDS300).² This dataset consists of 300 real-world images. The average segmentation results are listed in Table IV. The sampled cases are shown

²<https://www2.eecs.berkeley.edu/Research/Projects/CS/vision/bsds/BSDS300/html/dataset/images.html>

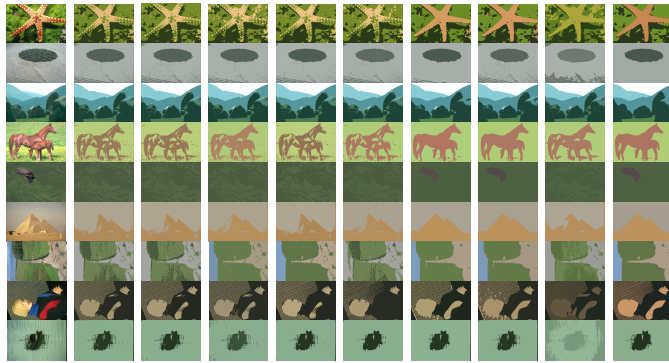


Fig. 11. Segmentation results on six color images in BSDS300. The parameters: $\alpha_1 = 0.5$, $\beta_1 = 15\,000$; $\alpha_2 = 0.5$, $\beta_2 = 15\,000$; $\alpha_3 = 0.8$, $\beta_3 = 25\,000$; $\alpha_4 = 0.8$, $\beta_4 = 10\,000$; $\alpha_5 = 0.5$, $\beta_5 = 15\,000$; $\alpha_6 = 0.7$, $\beta_6 = 25\,000$; $\alpha_7 = 0.5$, $\beta_7 = 10\,000$; $\alpha_8 = 0.8$; $\beta_8 = 20\,000$; and $\alpha_9 = 0.5$, $\beta_9 = 10\,000$. From left to right: original images and results of FCM_S1, FCM_S2, FGFCM, FLICM, KWFLICM, FRFCM, WFCM, DSFCM_N, and KLDPCM.

TABLE V

AVERAGE SEGMENTATION RESULTS ON REAL-WORLD IMAGES IN NEO

Method	EI	PC	PE	XB
FCM_S1	1.1854	0.9316	0.5285	0.0830
FCM_S2	1.1773	0.9355	0.5072	0.0825
FGFCM	1.1975	0.9318	0.5475	0.0880
FLICM	1.1748	0.9414	0.4936	0.0855
KWFLICM	1.1657	0.9435	0.4506	0.0851
FRFCM	1.0925	0.9699	0.2568	0.0744
WFCM	1.1063	0.9655	0.2855	0.0783
DSFCM_N	1.1895	0.9264	0.5385	0.0872
KLDPCM	1.0445	0.9823	0.1566	0.0374

in Fig. 11. Obviously, except for FRFCM and WFCM, other comparative algorithms perform poorly. Although FRFCM and WFCM mostly retain image contours, they result in several shape changes. Superior to them, the segmentation results of KLDPCM are closer to true segmentation results. Table IV illustrates that the quantitative results of KLDPCM are everywhere better than those of its peers, which indicates that KLDPCM acquires better uniformity in segmented images. Therefore, we conclude that KLDPCM can achieve excellent performance for segmenting real-world images.

Besides BSDS300, we consider segmenting real-world images coming from the NASA Earth observation database (NEO).³ In general, there exists unknown noise in sampled images due to bit errors appearing in satellite measurements. We choose two real-world images representing two specific scenes, that is, sea ice and snow extent and chlorophyll concentration. Due to the lack of reference (original) images, index EI cannot directly used. Hence, we randomly shoot each scene for 50 times within the time span 2000–2019, which generates the mean image. It can be taken as the reference image. The calculated EI, PC, PE, and XB results are given in Table V. The corresponding visual comparisons are presented in Fig. 12.

The first two rows of Fig. 12 report the segmentation results on a real-world image showing sea ice and snow extent. The colors show where the land and ocean are covered by snow and ice per week (here is February 7–14, 2015). We set $c = 4$.

³<http://neo.sci.gsfc.nasa.gov/>

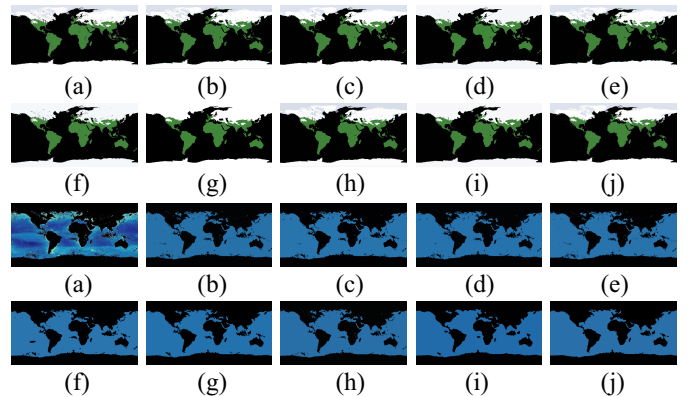


Fig. 12. Segmentation results on two real-world images ($\alpha_1 = 1.5$, $\beta_1 = 10\,000$ and $\alpha_2 = 1$, $\beta_2 = 15\,000$). From (a) to (j): noisy images and results of FCM_S1, FCM_S2, FGFCM, FLICM, KWFLICM, FRFCM, WFCM, DSFCM_N, and KLDPCM.

The last two rows of Fig. 12 illustrate the results for segmenting a real-world image showing chlorophyll concentration. The colors represent where and how much phytoplankton are growing over a span of days. The black areas show where the satellite could not measure phytoplankton. We set $c = 2$. As shown in Fig. 12, there exists the remaining noise in the segmented results of FCM_S1, FCM_S2, FGFCM, FLICM, KWFLICM, and WFCM. Although FRFCM and DSFCM_N can sufficiently remove unknown noise they give rise to over-smoothing to some extent. What is worse, there exist several topological changes, including merging and splitting in the segmentation results of the two algorithms. Compared with other peers, KLDPCM not only fully removes unknown noise, but also remains clear edges in images. In the light of the visual results shown in Fig. 12 and quantitative comparisons in Table V, it is concluded that KLDPCM overcomes the drawback of other FCM-related algorithms. Based on BSDS300 and NEO, when segmenting real-world images, the average SA improvement of KLDPCM over its peers is 4.41%.

F. Computing Overhead

To illustrate the efficiency of above FCM-related algorithms, we compare the computing overhead of KLDPCM with those of its peers. For fair comparison, we clarify that all experiments are completed in MATLAB on a laptop with Intel Xeon W-2133 CPU of (3.60 GHz) and 32.0-GB RAM. More specifically, we here demonstrate the average computing overheads of copying with different types of images, including synthetic, medical, and real-world images. The relevant results are shown in Fig. 13.

As shown in Fig. 13, when segmenting gray images, FLICM and KWFLICM are time-consuming. In comparison, the remaining algorithms present sound computational efficiency. Especially, FRFCM is the most time-efficient due to its usage of gray level histograms. Except for FRFCM, the efficiency of KLDPCM is higher than those of all other peers. As to color image segmentation, it is apparent that KWFLICM is the most time-consuming. Compared with other algorithms, FCM_S1, FCM_S2, FGFCM, WFCM, FRFCM,

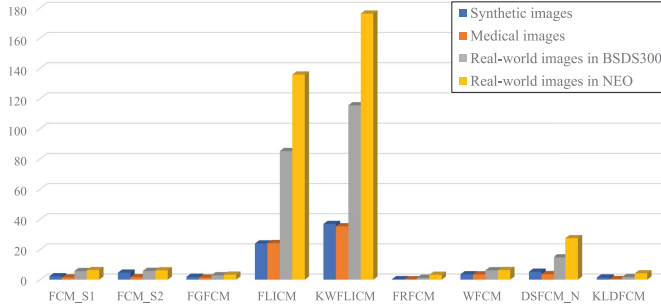


Fig. 13. Average computing overheads (in seconds) for different types of images.

and KLDFCM exhibit lower computational complexities. It is worth noting that the efficiency of KLDFCM is slightly lower than that of FGFCM and FRFCM. However, the drawback can be tolerated due to its better segmentation effects. Therefore, KLDFCM is more practical since it has acceptable computing overhead and better segmentation performance.

V. CONCLUSION

To retain a meaningful tradeoff between the segmentation performance and the speed of clustering, we have reported a KLDFCM algorithm by incorporating a tight wavelet frame transform and morphological reconstruction (MR). At the inception, an observed image is filtered by using MR. A tight wavelet frame system is employed to decompose the observed and filtered images so as to form their feature sets. Taking these feature sets as data of clustering, we present the modified FCM algorithm that incorporates a KL divergence term in the partition matrix into its objective function. Whereafter, we design a reconstruction process on the segmented feature set. As a result, the segmentation accuracy of KLDFCM is further improved. Moreover, we provide supporting experiments to show its effectiveness. The results illustrate that it is effective and practical. However, there are some open issues worth pursuing. For instance, the application areas of the proposed algorithm can be expanded to image segmentation in nonflat domains, such as remote sensing, computer networks, ecological systems, and transportation networks [46]–[51]. The values of the parameters might also be automatically chosen by using intelligent optimizations [52]–[55]. Moreover, the automatic setting of numbers of clusters can be further discussed.

APPENDIX

Consider the minimization of the objective function

$$J(\mathbf{U}, \mathbf{V}) = \sum_{i=1}^c \sum_{j=1}^K u_{ij} (\|x_j - v_i\|^2 + \alpha \|x_j - \bar{x}_j\|^2) + \beta \sum_{i=1}^c \sum_{j=1}^K u_{ij} \log \frac{u_{ij}}{\bar{u}_{ij}}$$

subject to

$$\sum_{i=1}^c u_{ij} = 1 \text{ for } j \in \{1, 2, \dots, K\}.$$

We apply the Lagrangian multiplier method to solve the minimization problem. The Lagrangian function is

formulated as

$$\mathcal{L}_\Lambda(\mathbf{U}, \mathbf{V}) = \sum_{i=1}^c \sum_{j=1}^K u_{ij} d_{ij} + \beta \sum_{i=1}^c \sum_{j=1}^K u_{ij} \log \frac{u_{ij}}{\bar{u}_{ij}} + \sum_{j=1}^K \lambda_j \left(\sum_{i=1}^c u_{ij} - 1 \right) \quad (12)$$

where $\Lambda = \{\lambda_j : j = 1, 2, \dots, K\}$ stands for a set of the Lagrangian multipliers, and $d_{ij} = \|x_j - v_i\|^2 + \alpha \|x_j - \bar{x}_j\|^2$.

First, by fixing \mathbf{V} , we minimize (12) in terms of the partition matrix \mathbf{U} . Thus, we have

$$\frac{\partial \mathcal{L}_\Lambda}{\partial u_{ij}} = d_{ij} + \beta \left(\log \frac{u_{ij}}{\bar{u}_{ij}} + 1 \right) + \lambda_j = 0.$$

We obtain

$$u_{ij} = \bar{u}_{ij} e^{-d_{ij}/\beta} \cdot \frac{1}{e^{\lambda_j/\beta+1}}. \quad (13)$$

Based on the constraint $\sum_{q=1}^c u_{qj} = 1$, we have

$$\begin{aligned} 1 &= \sum_{q=1}^c u_{qj} = \sum_{q=1}^c \left(\bar{u}_{qj} e^{-d_{qj}/\beta} \cdot \frac{1}{e^{\lambda_j/\beta+1}} \right) \\ &= \frac{1}{e^{\lambda_j/\beta+1}} \sum_{q=1}^c \bar{u}_{qj} e^{-d_{qj}/\beta}. \end{aligned}$$

Thus, we obtain

$$\frac{1}{e^{\lambda_j/\beta+1}} = 1 / \sum_{q=1}^c \bar{u}_{qj} e^{-d_{qj}/\beta}. \quad (14)$$

Substituting (14) into (13), we acquire

$$u_{ij} = \frac{\bar{u}_{ij} e^{-d_{ij}/\beta}}{\sum_{q=1}^c \bar{u}_{qj} e^{-d_{qj}/\beta}}.$$

Next, by fixing \mathbf{U} , we minimize (12) in terms of \mathbf{V} . Thus, we have

$$\frac{\partial \mathcal{L}_\Lambda}{\partial v_i} = \sum_{j=1}^K (-2) \cdot u_{ij} \cdot ((x_j + \alpha \bar{x}_j) - (v_i + \alpha v_i)) = 0.$$

With that

$$\sum_{j=1}^K u_{ij} (x_j + \alpha \bar{x}_j) = \sum_{j=1}^K u_{ij} (v_i + \alpha v_i).$$

The optimal v_i is described as

$$v_i = \frac{\sum_{j=1}^K u_{ij} (x_j + \alpha \bar{x}_j)}{(1 + \alpha) \sum_{j=1}^K u_{ij}}.$$

REFERENCES

- [1] J. C. Dunn, "A fuzzy relative of the ISODATA process and its use in detecting compact well-separated clusters," *J. Cybern.*, vol. 3, no. 3, pp. 32–57, 1973.
- [2] J. C. Bezdek, *Pattern Recognition With Fuzzy Objective Function Algorithms*. New York, NY, USA: Plenum Press, 1981.
- [3] L. Szilagyi, Z. Benyo, S. Szilagyi, and H. S. Adam, "MR brain image segmentation using an enhanced Fuzzy C-Means algorithm," in *Proc. 25th Annu. Int. Conf. IEEE Eng. Med. Biol. Soc. (EMBS)*, Cancun, Mexico, Sep. 2003, pp. 724–726.
- [4] X. Zhu, W. Pedrycz, and Z. Li, "Granular encoders and decoders: A study in processing information granules," *IEEE Trans. Fuzzy Syst.*, vol. 25, no. 5, pp. 1115–1126, Oct. 2017.

- [5] T. Celik and H. K. Lee, "Comments on 'A robust fuzzy local information c-means clustering algorithm'" *IEEE Trans. Image Process.*, vol. 22, no. 3, pp. 1258–1261, Mar. 2013.
- [6] M. N. Ahmed, S. M. Yamany, N. Mohamed, A. A. Farag, and T. Moriarty, "A modified fuzzy C-means algorithm for bias field estimation and segmentation of MRI data," *IEEE Trans. Med. Imag.*, vol. 21, no. 3, pp. 193–199, Mar. 2002.
- [7] S. Chen and D. Zhang, "Robust image segmentation using FCM with spatial constraints based on new kernel-induced distance measure," *IEEE Trans. Syst., Man, Cybern. B, Cybern.*, vol. 34, no. 4, pp. 1907–1916, Aug. 2004.
- [8] W. Cai, S. Chen, and D. Zhang, "Fast and robust fuzzy c -means clustering algorithms incorporating local information for image segmentation," *Pattern Recognit.*, vol. 40, no. 3, pp. 825–838, Mar. 2007.
- [9] S. Krinidis and V. Chatzis, "A robust fuzzy local information C-means clustering algorithm," *IEEE Trans. Image Process.*, vol. 19, no. 5, pp. 1328–1337, May 2010.
- [10] X. Bai, Y. Zhang, H. Liu, and Z. Chen, "Similarity measure-based possibilistic FCM with label information for brain MRI segmentation," *IEEE Trans. Cybern.*, vol. 49, no. 7, pp. 2618–2630, Jul. 2019.
- [11] M. Gong, Y. Liang, J. Shi, W. Ma, and J. Ma, "Fuzzy C-Means clustering with local information and kernel metric for image segmentation," *IEEE Trans. Image Process.*, vol. 22, no. 2, pp. 573–584, Feb. 2013.
- [12] Z. Zhao, L. Cheng, and G. Cheng, "Neighbourhood weighted fuzzy C-means clustering algorithm for image segmentation," *IET Image Process.*, vol. 8, no. 3, pp. 150–161, Mar. 2014.
- [13] C. Wang, W. Pedrycz, J. Yang, M. Zhou, and Z. Li, "Wavelet frame-based fuzzy C-means clustering for segmenting images on graphs," *IEEE Trans. Cybern.*, vol. 50, no. 9, pp. 3938–3949, Sep. 2020.
- [14] K.-P. Lin, "A novel evolutionary kernel intuitionistic fuzzy C-means clustering algorithm," *IEEE Trans. Fuzzy Syst.*, vol. 22, no. 5, pp. 1074–1087, Oct. 2014.
- [15] X. Zhu, W. Pedrycz, and Z. W. Li, "Fuzzy clustering with nonlinearly transformed data," *Appl. Soft Comput.*, vol. 61, pp. 364–376, Dec. 2017.
- [16] R. R. Gharieb, G. Gendy, A. Abdelfattah, and H. Selim, "Adaptive local data and membership based KL divergence incorporating C-means algorithm for fuzzy image segmentation," *Appl. Soft Comput.*, vol. 59, pp. 143–152, Oct. 2017.
- [17] C. Wang, W. Pedrycz, Z. Li, M. Zhou, and S. S. Ge, "G-image segmentation: Similarity-preserving fuzzy C-means with spatial information constraint in wavelet space," *IEEE Trans. Fuzzy Syst.*, early access, Oct. 7, 2020, doi: [10.1109/TFUZZ.2020.3029285](https://doi.org/10.1109/TFUZZ.2020.3029285).
- [18] T. Lei, X. Jia, Y. Zhang, L. He, H. Meng, and A. K. Nandi, "Significantly fast and robust Fuzzy C-Means clustering algorithm based on morphological reconstruction and membership filtering," *IEEE Trans. Fuzzy Syst.*, vol. 26, no. 5, pp. 3027–3041, Oct. 2018.
- [19] C. Wang, W. Pedrycz, Z. Li, M. Zhou, and J. Zhao, "Residual-sparse Fuzzy C-Means clustering incorporating morphological reconstruction and wavelet frame," *IEEE Trans. Fuzzy Syst.*, early access, Oct. 7, 2020, doi: [10.1109/TFUZZ.2020.3029296](https://doi.org/10.1109/TFUZZ.2020.3029296).
- [20] C. Wang, W. Pedrycz, M. Zhou, and Z. Li, "Sparse regularization-based Fuzzy C-Means clustering incorporating morphological grayscale reconstruction and wavelet frames," *IEEE Trans. Fuzzy Syst.*, vol. 29, no. 7, pp. 1826–1840, Jul. 2021.
- [21] J. Gu, L. Jiao, S. Yang, and F. Liu, "Fuzzy double C-means clustering based on sparse self-representation," *IEEE Trans. Fuzzy Syst.*, vol. 26, no. 2, pp. 612–626, Apr. 2018.
- [22] Y. Zhang, X. Bai, R. Fan, and Z. Wang, "Deviation-sparse fuzzy C-means with neighbor information constraint," *IEEE Trans. Fuzzy Syst.*, vol. 27, no. 1, pp. 185–199, Jan. 2019.
- [23] C. Wang, W. Pedrycz, Z. Li, and M. Zhou, "Residual-driven fuzzy C-means clustering for image segmentation," *IEEE/CAA J. Autom. Sinica*, vol. 8, no. 4, pp. 876–889, Apr. 2021.
- [24] X. Jia, T. Lei, P. Liu, D. Xue, H. Meng, and A. K. Nandi, "Fast and automatic image segmentation using superpixel-based graph clustering," *IEEE Access*, vol. 8, pp. 211526–211539, 2020.
- [25] T. Lei, P. Liu, X. Jia, X. Zhang, H. Meng, and A. K. Nandi, "Automatic fuzzy clustering framework for image segmentation," *IEEE Trans. Fuzzy Syst.*, vol. 28, no. 9, pp. 2078–2092, Sep. 2020.
- [26] J.-F. Cai, B. Dong, S. Osher, and Z. Shen, "Image restoration: Total variation, wavelet frames, and beyond," *J. Amer. Math. Soc.*, vol. 25, no. 4, pp. 1033–1089, May 2012.
- [27] B. Dong and Z. Shen, "MRA-based wavelet frames and applications," in *The Mathematics of Image Processing* (IAS Lecture Notes Series). Salt Lake City, UT, USA: Park City Math. Inst., 2010.
- [28] L. Najman and M. Schmitt, "Geodesic saliency of watershed contours and hierarchical segmentation," *IEEE Trans. Pattern Anal. Mach. Intell.*, vol. 18, no. 12, pp. 1163–1173, Dec. 1996.
- [29] L. Vincent, "Morphological grayscale reconstruction in image analysis: Applications and efficient algorithms," *IEEE Trans. Image Process.*, vol. 2, no. 2, pp. 176–201, Apr. 1993.
- [30] J. C. Bezdek, R. Ehrlich, and W. Full, "FCM: The fuzzy C -means clustering algorithm," *Comput. Geosci.*, vol. 10, nos. 2–3, pp. 191–203, 1984.
- [31] B. Dong, "Sparse representation on graphs by tight wavelet frames and applications," *Appl. Comput. Harmon. Anal.*, vol. 42, no. 3, pp. 452–479, May 2017.
- [32] C. Wang, Z. Yan, W. Pedrycz, M. Zhou, and Z. Li, "A weighted fidelity and regularization-based method for mixed or unknown noise removal from images on graphs," *IEEE Trans. Image Process.*, vol. 29, pp. 5229–5243, 2020.
- [33] C. Wang and J. Yang, "Poisson noise removal of images on graphs using tight wavelet frames," *Visual Comput.*, vol. 34, no. 10, pp. 1357–1369, Oct. 2018.
- [34] B. Dong, Q. T. Jiang, C. Q. Liu, and Z. Shen, "Multiscale representation of surfaces by tight wavelet frames with applications to denoising," *Appl. Comput. Harmon. Anal.*, vol. 41, no. 2, pp. 561–589, Sep. 2016.
- [35] J. Yang and C. Wang, "A wavelet frame approach for removal of mixed Gaussian and impulse noise on surfaces," *Inverse Problem Imag.*, vol. 11, no. 5, pp. 783–798, Oct. 2017.
- [36] A. Ron and Z. Shen, "Affine systems in $L_2(\mathbb{R}^d)$: The analysis of the analysis operator," *J. Funct. Anal.*, vol. 148, no. 2, pp. 408–447, Aug. 1997.
- [37] J.-J. Chen, C.-R. Su, W. E. L. Grimson, J.-L. Liu, and D.-H. Shiu, "Object segmentation of database images by dual multiscale morphological reconstructions and retrieval applications," *IEEE Trans. Image Process.*, vol. 21, no. 2, pp. 828–843, Feb. 2012.
- [38] J. Yang, G. Zhu, D. Tong, L. Lu, and Z. Shen, "B-spline tight frame based force matching method," *J. Comput. Phys.*, vol. 362, no. 1, pp. 208–219, Jun. 2018.
- [39] D. N. H. Thanh, D. Sergey, V. B. S. Prasath, and N. H. Hai, "Blood vessels segmentation method for retinal fundus images based on adaptive principal curvature and image derivative operators," *Int. Arch. Photogramm. Remote Sens. Spatial Inf. Sci.*, vol. XLII-2/W12, pp. 211–218, May 2019, doi: [10.5194/isprs-archives-XLII-2-W12-211-2019](https://doi.org/10.5194/isprs-archives-XLII-2-W12-211-2019).
- [40] D. N. H. Thanh, U. Erkan, V. B. S. Prasath, V. Kumar, and N. N. Hien, "A skin lesion segmentation method for dermoscopic images based on adaptive thresholding with normalization of color models," in *Proc. IEEE 6th Int. Conf. Electr. Electron. Eng.*, Istanbul, Turkey, Apr. 2019, pp. 116–120.
- [41] A. A. Taha and A. Hanbury, "Metrics for evaluating 3D medical image segmentation: Analysis, selection, and tool," *BMC Med. Imag.*, vol. 15, no. 29, pp. 1–29, Aug. 2015.
- [42] H. Zhang, J. Fritts, and S. Goldman, "An entropy-based objective evaluation method for image segmentation," in *Proc. SPIE Storage Retrieval Methods Appl. Multimedia*, vol. 5307, Jan. 2004, pp. 38–49.
- [43] O. Arbelaitz, I. Gurrutxaga, J. Muguerza, J. M. Pérez, and I. Perona, "An extensive comparative study of cluster validity indices," *Pattern Recognit.*, vol. 46, no. 1, pp. 243–256, Jan. 2013.
- [44] X. L. Xie and G. Beni, "A validity measure for fuzzy clustering," *IEEE Trans. Pattern Anal. Mach. Intell.*, vol. 13, no. 8, pp. 841–847, Aug. 1991.
- [45] T. Lei, Y. Zhang, Y. Wang, S. Liu, and Z. Guo, "A conditionally invariant mathematical morphological framework for color images," *Inf. Sci.*, vol. 387, pp. 34–52, May 2017.
- [46] T. Xu, L. Jiao, and W. J. Emery, "SAR image content retrieval based on fuzzy similarity and relevance feedback," *IEEE J. Sel. Topics Appl. Earth Observ. Remote Sens.*, vol. 10, no. 5, pp. 1824–1842, May 2017.
- [47] C. Wang, J. Chen, Z. Li, E. Nasr, and A. M. El-Tamimi, "An indicator system for evaluating the development of land-sea coordination systems: A case study of Lianyungang port," *Ecol. Indicators*, vol. 98, pp. 112–120, Mar. 2019.
- [48] M. Ghahramani, M. Zhou, and G. Wang, "Urban sensing based on mobile phone data: approaches, applications, and challenges," *IEEE/CAA J. Autom. Sinica*, vol. 7, no. 3, pp. 627–637, May 2020.
- [49] A. K. Bhandari, A. Ghosh, and I. V. Kumar, "A local contrast fusion based 3D Otsu algorithm for multilevel image segmentation," *IEEE/CAA J. Autom. Sinica*, vol. 7, no. 1, pp. 200–213, Jan. 2020.

- [50] Y. Xia, H. Yu, and F.-Y. Wang, "Accurate and robust eye center localization via fully convolutional networks," *IEEE/CAA J. Autom. Sinica*, vol. 6, no. 5, pp. 1127–1138, Sep. 2019.
- [51] Z. Cao, X. Xu, B. Hu, and M. Zhou, "Rapid detection of blind roads and crosswalks by using a lightweight semantic segmentation network," *IEEE Trans. Intell. Transp. Syst.*, early access, May 14, 2020, doi: [10.1109/TITS.2020.2989129](https://doi.org/10.1109/TITS.2020.2989129).
- [52] W. Dong and M. Zhou, "Gaussian classifier-based evolutionary strategy for multimodal optimization," *IEEE Trans. Neural Net. Learn. Syst.*, vol 25, no. 6, pp. 1200–1216, Jun. 2014.
- [53] M. Shang, Y. Yuan, X. Luo, and M. Zhou, "An α - β -divergence-generalized recommender for highly accurate predictions of missing user preferences," *IEEE Tran. Cybern.*, early access, Feb. 18, 2020, doi: [10.1109/TCYB.2020.3026425](https://doi.org/10.1109/TCYB.2020.3026425).
- [54] G. Tian, Y. Ren, and M. Zhou, "Dual-objective scheduling of rescue vehicles to distinguish forest fires via differential evolution and particle swarm optimization combined algorithm," *IEEE Trans. Intell. Transp. Syst.*, vol. 17, no. 11, pp. 3009–3021, Nov. 2016.
- [55] X. Guo, S. Liu, G. Tian, and M. Zhou, "Disassembly sequence optimization for large-scale products with multiresource constraints using scatter search and Petri nets," *IEEE Trans. Cybern.*, vol. 46, no. 11, pp. 2435–2446, Nov. 2016.



Cong Wang (Member, IEEE) received the B.S. degree in automation and the M.S. degree in mathematics from Hohai University, Nanjing, China, in 2014 and 2017, respectively, and the Ph.D. degree in mechatronic engineering from Xidian University, Xi'an, China, in 2021.

He is currently an Assistant Professor with the School of Artificial Intelligence, Optics and Electronics, Northwestern Polytechnical University, Xi'an, China. He was a visiting Ph.D. student with the Department of Electrical and Computer Engineering, University of Alberta, Edmonton, AB, Canada, and the Department of Electrical and Computer Engineering, National University of Singapore, Singapore. He was also a Research Assistant with the School of Computer Science and Engineering, Nanyang Technological University, Singapore. His current research interests include wavelet analysis and its applications, fuzzy theory, granular computing, as well as image processing.

Witold Pedrycz (Life Fellow, IEEE) received the M.Sc. degree in computer science and technology, the Ph.D. degree in computer engineering, and the D.Sci. degree in systems science from the Silesian University of Technology, Gliwice, Poland, in 1977, 1980, and 1984, respectively. He is a Foreign Member of the Polish Academy of Sciences. He has authored 15 research monographs covering various aspects of computational intelligence, data mining, and software engineering. His current research interests include computational intelligence, fuzzy modeling and granular computing, knowledge discovery and data mining, fuzzy control, pattern recognition, knowledge-based neural networks, relational computing, and software engineering. He has published numerous papers in the above areas.

Prof. Pedrycz was a recipient of the IEEE Canada Computer Engineering Medal, the Cajastur Prize for Soft Computing from the European Centre for Soft Computing, the Killam Prize, and the Fuzzy Pioneer Award from the IEEE Computational Intelligence Society. He is extensively involved in editorial activities. He is the Editor-in-Chief of *Information Sciences*, *WIREs Data Mining and Knowledge Discovery* (Wiley), and the *International Journal of Granular Computing* (Springer). He currently serves as a member of a number of editorial boards of other international journals. He is a Fellow of the Royal Society of Canada.



ZhiWu Li (Fellow, IEEE) received the B.S. degree in mechanical engineering, the M.S. degree in automatic control, and the Ph.D. degree in manufacturing engineering from Xidian University, Xi'an, China, in 1989, 1992, and 1995, respectively.

He joined Xidian University in 1992. He is also currently with the Institute of Systems Engineering, Macau University of Science and Technology, Macau, China. He was a Visiting Professor with the University of Toronto, Toronto, ON, Canada; the Technion-Israel Institute of Technology, Haifa, Israel; the Martin-Luther University of Halle-Wittenberg, Halle, Germany; Conservatoire National des Arts et Métiers, Paris, France; and Meliksah Universitesi, Kayseri, Turkey. His current research interests include Petri net theory and application, supervisory control of discrete-event systems, workflow modeling and analysis, system reconfiguration, game theory, and data and process mining.

Dr. Li was a recipient of the Alexander von Humboldt Research Grant, Alexander von Humboldt Foundation, Germany. He is listed in Marquis *Who's Who in the World*, 27th Edition, 2010. He serves as a frequent reviewer of 90+ international journals, including *Automatica* and a number of the IEEE TRANSACTIONS as well as many international conferences. He is the Founding Chair of Xi'an Chapter of the IEEE Systems, Man, and Cybernetics Society. He is a member of Discrete-Event Systems Technical Committee of the IEEE Systems, Man, and Cybernetics Society and IFAC Technical Committee on Discrete-Event and Hybrid Systems from 2011 to 2014.



MengChu Zhou (Fellow, IEEE) received the B.S. degree in control engineering from the Nanjing University of Science and Technology, Nanjing, China, in 1983, the M.S. degree in automatic control from the Beijing Institute of Technology, Beijing, China, in 1986, and the Ph.D. degree in computer and systems engineering from Rensselaer Polytechnic Institute, Troy, NY, USA, in 1990.

He joined the New Jersey Institute of Technology, Newark, NJ, USA, in 1990, where he is currently a Distinguished Professor of Electrical and Computer Engineering. He has over 900 publications, including 12 books, 600+ journal papers (500+ in IEEE TRANSACTIONS), 29 patents, and 29 book-chapters. His recently co-authored/edited books include *Supervisory Control and Scheduling of Resource Allocation Systems: Reachability Graph Perspective*, IEEE Press/Wiley, Hoboken, Hoboken, New Jersey J, 2020 (with B. Huang) and *Contemporary Issues in Systems Science and Engineering*, IEEE/Wiley, Hoboken, New Jersey, 2015 (with H.-X. Li and M. Weijnen). His research interests are in Petri nets, intelligent automation, Internet of Things, big data, Web services, and intelligent transportation.

Dr. Zhou is a recipient of the Humboldt Research Award for U.S. Senior Scientists from Alexander von Humboldt Foundation, the Franklin V. Taylor Memorial Award, and the Norbert Wiener Award from IEEE Systems, Man and Cybernetics Society. He has been among most highly cited scholars for years and ranked top one in the field of engineering worldwide in 2012 by Web of Science/Thomson Reuters and now Clarivate Analytics. He is the founding Chair/Co-Chair of Enterprise Information Systems Technical Committee (TC), Environmental Sensing, Networking, and Decision-Making TC, and AI-based Smart Manufacturing Systems TC of IEEE SMC Society. He is the Founding Editor of IEEE Press Book Series on Systems Science and Engineering and the Editor-in-Chief of *IEEE/CAA JOURNAL OF AUTOMATICA SINICA*. He is a Life Member of Chinese Association for Science and Technology-USA and served as its President in 1999. He is a Fellow of the International Federation of Automatic Control, the American Association for the Advancement of Science, the Chinese Association of Automation, and the National Academy of Inventors.